The competition between frequent and rare flood events: impacts on erosion rates and landscape form

J. M. Adams[1,2], N. M. Gasparini[2], G. E. Tucker[3,4], E. Istanbulluoglu[5]

[1]Division of Science and Math, Delgado Community College, New Orleans, LA, USA
[2]Department of Earth and Environmental Sciences, Tulane University, New Orleans, LA, USA
[3]Department of Geological Sciences, University of Colorado Boulder, Boulder, CO, USA
[4]Cooperative Institute for Research in Environmental Sciences, University of Colorado Boulder, Boulder, CO, USA
[5]Department of Civil and Environmental Engineering, University of Washington, Seattle, WA, USA

1 Abstract

Runoff variability plays an important role in landscape evolution. Previous work has shown that with increased climatic variability there are simultaneous increases in the likelihood of geomorphically-effective floods that shape watershed morphology. Numerical models have been applied to explore these patterns, but often assume hydrologic steady-state, neglecting the dynamics and erosional impact of an event hydrograph. This study uses a stochastic storm generator and new overland flow method to generate and route individual event hydrographs for two storm time series: a high variability climate time series characterized by short-duration, high-intensity storms, and a low variability climate time series, characterized by longer duration, lower-intensity storms. Using steady and nonsteady hydrology methods, detachment-limited erosion rates are calculated using a range of critical shear stresses. Erosion results illustrate that when no critical shear stress is considered, storms in the lower variability climate scenario drive greater overall erosion than the higher variability case. However, as the critical shear stress or entrainment threshold is increased, the higher variability climate achieves a greater erosive power. Landscape sensitivity to climate is similar between the two discharge methods, but the erosional patterns are distinct, as erosion rates calculated using the nonsteady discharge method are more sensitive to changes in storm characteristics. This sensitivity varies spatially, as the event hydrograph duration changes with drainage area, driving significant downstream increases in erosion rates and depth. Results from this work indicate that the erosional influence of a hydrograph may be important to consider when exploring the impact of climatic variability on landscape evolution.

2 Introduction

The groundbreaking work of *Wolman and Miller* [1960] spurred extensive discussion in the field of fluvial geomorphology about the frequency and magnitude of flood events, and how the geomorphic work of these floods sculpts landscapes. Large storm-driven flood events capable of transporting sediment cover and eroding into bedrock are rare [e.g. *Molnar*, 2001; *Lague et al.*, 2005; *Molnar et al.*, 2006; *Turowski et al.*, 2008], while more frequent, moderate events maintain channel form [*Wolman and Gerson*, 1978; *Miller*, 1990; *Costa and O'Connor*, 1995; *Hartshorn et al.*, 2002; *Guthrie*, 2015; *Phillips and Jerolmack*, 2016]. For example, it has been shown that rivers 'self-organize' in response to bankfull floods, suggesting these moderate events are more important in setting channel geometries than infrequent or intense flood events [*Phillips and Jerolmack*, 2016].

Considerable literature has explored the climatic drivers of geomorphic work, where variability in rainfall and discharge are modeled to evaluate the erosive imprint of flood events. Many studies have demonstrated that climatic variability can play a significant role in the formation and evolution of landscapes [e.g. *Tucker and Bras*, 2000; *Tucker*, 2004; *Snyder et al.*, 2003; *Lague et al.*, 2005; *DiBiase and Whipple*, 2011; *Lague*, 2014; *Rossi et al.*, 2016; *Deal et al.*, 2017, 2018]. Using a landscape evolution model, *Tucker and Bras* [2000] illustrated that sediment transport rates increase with rainfall variability, whereas detachment-limited incision rates have a more nuanced response. In their model, detachment-limited

incision rates may increase or decrease as a function of rainfall variability and the nonlinearity of the shear stress equation [*Tucker and Bras*, 2000]. Other models driven by climatic variability have demonstrated that changes in flood frequency, relative to the selected entrainment threshold, may also be responsible for increased erosion rates that influence landscape form [*Tucker*, 2004]. Modeled landscapes evolved with rainfall or discharge variability have greater drainage densities and overall reduced relief [*Tucker and Bras*, 2000]. Channel steepness can also be controlled by discharge variability, in particular when lithologies are weak and incision rates are low [*Snyder et al.*, 2003; *Lague et al.*, 2005].

Because landscape characteristics are sensitive to climatic variability, it is important to consider that variability when interpreting past and current landscape form or predicting future landscape change. In particular, landscape response to rainfall and discharge variability can be important when exploring how incision rates change in response to climate change. For example, *Molnar* [2001] and *Molnar et al.* [2006] explored how predicted aridification, driven by climate change, may affect incision rates. While the aridification of a landscape may drive larger, more erosive flooding events [*Molnar*, 2001], whether incision rates increase or decrease is determined by a threshold discharge, below which no incision can occur [*Lague et al.*, 2005; *Molnar et al.*, 2006]. The distribution of rainfall and discharge determines the probability a given flood or storm will exceed that threshold discharge, and therefore determines the probability an erosive event occurs [*Tucker and Bras*, 2000; *Lague et al.*, 2005; *Molnar et al.*, 2006; *DiBiase and Whipple*, 2011; *Rossi et al.*, 2016; *Deal et al.*, 2017, 2018].

Numerical models are often applied to understand the role of rainfall variability in landscape evolution, but often with some limitations or constraints. Many landscape evolution models simplify rainfall and discharge processes into a single value that is temporally constant during a model simulation. Other models that incorporate stochastic rainfall may calculate temporally uniform discharge rates for each given storm event [e.g. *Tucker and Bras*, 2000; *Sólyom and Tucker*, 2004; *Attal et al.*, 2008, 2011]. Both discharge methods neglect the impact of a storm hydrograph, and how erosion is integrated as a function of variable discharge throughout a storm hydrograph. If a physically-based hydrograph routing method is used instead of a single-value approach, output topographies may have different morphological characteristics, such as increased relief or reduced concavities [e.g. *Adams et al.*, 2017], suggesting that capturing rainfall and discharge variability in more detail may be important to understand landscape evolution [*Tucker and Hancock*, 2010].

In this study, we use a novel modeling method that explores rainfall variability, hydrograph generation and fluvial erosion across different climatic regimes. To simulate flooding and erosion across a synthetic landscape, a stochastic rainfall generator [e.g. *Eagleson*, 1978; *Hawk*, 1992; *Tucker and Bras*, 2000] is coupled with an overland flow component in the Landlab modeling framework [*Adams et al.*, 2017; *Hobley et al.*, 2017]. Using this method, we explore the following questions: How does rainfall variability, as a proxy for climate, impact erosion rates? Do patterns in erosion rates change between the steady or nonsteady discharge methods? How do predictions of landscape sensitivity to climate compare across the different discharge methods? What are the implications for landscape morphology?

To understand the influence of variable rainfall and discharge, a stochastic rainfall generator is parameterized with data from two locations with similar mean annual precipitation, but differences in average storm depth, storm and interstorm durations. These storm time series provide two endmember cases: a high variability rainfall time series, where storms are infrequent but intense; and a low variability rainfall time series, where storms occur more frequently and with relatively lower intensities. Both storm distributions are used to initiate detachment-limited erosion across the model domain, and erosion rates are calculated with and without a critical shear stress threshold. For the different storm variability cases, total erosion depths are evaluated to explore how the cumulative work of floods controls watershed morphology.

This study agrees with findings of previous work, showing that when critical shear stress values are low, the cumulative impact of several high-frequency, low-magnitude rainfall events in temperate climates will be more effective at shaping watersheds than rare, high magnitude events in arid regimes [*Tucker*, 2004]. However, as the entrainment threshold increases, these results begin to shift, as low magnitude events are less capable of incising into the substrate, particularly in the lowest drainage areas and hillslopes. Results presented here illustrate how hydrograph shape and duration, storm characteristics not captured in many landscape evolution models, affect modeled landform shape. As hydrograph-driven erosion rates vary across a watershed, lower drainage areas are more sensitive to rainfall characteristics, particularly when considering entrainment thresholds. By modeling variability in rainfall and discharge processes, these results can be used to inform the ongoing discussion of the geomorphic effectiveness of different climatic regimes.

3 Methods

3.1 Model description

All modeling efforts described in this study used the open-source Landlab modeling framework [*Hobley et al.*, 2017]. The synthetic model domain was initialized as a rectangular mesh of square grid cells ($\Delta x = \Delta y = 50$ m) make up the 100 km^2 domain. At the center of these grid cells are nodes, which contain state variables such as topographic elevation and surface water depth. Nodes are connected to their neighbors by vectors called links. Fluxes, such as water discharge, are calculated and stored on the links.

The initial model topography was evolved with a constant rainfall rate, using three Landlab components that simulate steady D4 flow routing (FlowRouter), fluvial incision (FastscapeEroder) and linear hillslope diffusion (LinearDiffuser). Starting from initial random noise, the model domain was evolved to topographic steady state, to a condition where the uniform uplift rate is matched by the erosion rate. No flow can move cross the edges of the domain, except at the watershed outlet in southwest corner (Fig. 1).

For the suite of nonsteady flow routing experiments, overland flow and erosion processes are coupled within the Landlab modeling framework and applied across this synthetic domain to explore how different climate regimes can shape landscapes. For each suite of modeling scenarios, a stochastic storm generator (PrecipitationDistribution) is used to generate a rainfall time series. Rainfall parameters are passed to a nonsteady overland flow component (OverlandFlow) that calculates surface water discharge on grid links. Changes in surface water fluxes update the water depths on nodes. These changing water depths are passed to model methods which calculate spatially and temporally variable Manning's roughness coefficients. Water depths are also used to calculate erosion rate as a function of shear stress (DepthSlopeProductErosion), and linearly diffusive processes are simulated on hillslopes (LinearDiffuser). At the end of each time step, the topography is updated as a function of erosion and diffusion processes and tectonic uplift.

In later experiments, we use the same stochastic storm time series in a more traditional approach, routing steady discharge the resulting erosion across the same domain. These results are used to contrast patterns of fluvial incision between the steady and nonsteady flow routing methodologies. The background material and the equations used for these experiments are described in the following subsections. All variables and parameters are described in Tables (1) and (2).

3.1.1 Stochastic precipitation generator

The stochastic rainfall generator in Landlab (PrecipitationDistribution) is based on the rectangular Poisson pulse rainfall model [*Eagleson*, 1978; *Tucker and Bras*, 2000]. The Poisson method describes the probability a given storm event will happen. In this approach,

storms are treated as discrete events, with three characteristics generated from statistical distributions: t_r, storm duration [T]; t_b, interstorm duration [T]; and total rainfall depth, D [L]. Rainfall intensity P [LT^{-1}] can be solved as a function of total rainfall depth and storm duration. In an actual storm time series, there is variability in rainfall intensity throughout a storm (Fig. 2a). The rectangular Poisson model eliminates that variability, and instead creates an idealized precipitation time series that assumes that each storm has one constant intensity throughout the event (Fig. 2b). All storm events are temporally constant and spatially uniform across the model domain.

The PrecipitationDistribution generator is parameterized by the mean value of each of the rainfall characteristics: storm duration ($\overline{t_r}$), interstorm duration ($\overline{t_b}$) and rainfall depth ($\overline{d}$). *Hawk* [1992] compiled mean values for several sites across the United States. Using these mean values, storm events are drawn from different statistical distributions to create a rainfall time series. *Eagleson* [1978] demonstrated that storm and interstorm duration fit the Poisson distribution:

$$f(t_r) = \frac{1}{\overline{t_r}} e^{t_r/\overline{t_r}} \tag{1}$$

$$f(t_b) = \frac{1}{\overline{t_b}} e^{t_b/\overline{t_b}}. \tag{2}$$

Because rainfall depths are dependent on storm duration [*Grayman and Eagleson*, 1969], depths for each event are sampled from the gamma statistical distribution as a function of mean storm depth ($\overline{d}$) and sampled storm duration (t_r), following *Ivanov et al.* [2007]:

$$f(d) = \frac{1}{\overline{d}} \frac{\left(\frac{d}{\overline{d}}\right)^{(t_r/\overline{t_r})-1} e^{-d/\overline{d}}}{\Gamma\left(\frac{t_r}{\overline{t_r}}\right)}. \tag{3}$$

3.1.2 Overland flow routing

The Landlab OverlandFlow component can be used to route flood waves, by implementing a 2D diffusive approximation of the shallow water equations designed to work on gridded terrain data [*Bates et al.*, 2010; *de Almeida et al.*, 2012; *Adams et al.*, 2017]. The diffusive wave approximation assumes channels have rectangular cross-sectional areas, constant flow widths and that flow advection is negligible. Before calculating discharge, an adaptive time step is calculated following the Courant-Freidrichs-Lewy (CFL) condition. The time step depends on the grid resolution and flood wave speed. This method maximizes the computational efficiency of the model, and limits instabilities in model output. Following *Hunter et al.* [2005], the adaptive time step is calculated as:

$$\Delta t = \alpha \frac{\Delta x}{\sqrt{g h_{max}}} \tag{4}$$

where Δt is the maximum time step that adheres to the CFL condition [T]; α is a dimensionless stability coefficient; Δx is the grid resolution [L]; the wave celerity, or velocity of a shallow water wave, $\sqrt{g h_{max}}$ [LT^{-1}], is calculated using g, the acceleration due to gravity [LT^{-2}] and h_{max} [L], the maximum water depth within the modeling domain. At all time steps, a thin film of water is maintained across the modeling domain to keep this solution valid.

Water discharge on the surface of the domain is calculated from an explicit, centered solution [for derivation see *de Almeida et al.*, 2012]. The solution simulates a flood wave moving across the model domain, and surface water discharge is calculated as:

$$q_x^{t+\Delta t} = \frac{[\theta q_x^t + \frac{1-\theta}{2}(q_{(x-1)}^t + q_{(x+1)}^t)] - g h_{f(x)} \Delta t S_{w(x)}}{1 + g \Delta t n^2 |q_x^t|/h_f^{7/3}} \tag{5}$$

where q is water discharge per unit width $[L^2 T^{-1}]$ with superscript t for the model time step and subscript x describing the location in space. θ is a discharge weighting factor between 0 and 1; h_f is the local maximum water surface depth at a given time $[L]$; Δt is the adaptive time step (Eq. 4); S_w is the dimensionless water surface slope; and n is an array of spatially variable Manning's friction coefficient values $[L^{-1/3}T]$, used to distinguish hillslopes and channels within the model and described in more detail in the following section.

This equation restricts flow to a D4 routing scheme, directing flow in the four cardinal directions into or out of a given node. Changes in water discharge on links drive changes in water depths on the nodes. Updated water depths are calculated as:

$$\frac{\Delta h}{\Delta t} = \frac{Q_{h(in)} - Q_{h(out)}}{\Delta x \Delta y} \tag{6}$$

where $Q_{h(in)}$ are the summed volumetric water discharges moving into a given node and $Q_{h(out)}$ are summed volumetric water discharges moving out of a given node. Flow directions are determined by the local gradient of each link. During a precipitation event, input rainfall is added to the surface water depths mapped onto nodes. For more details on how this algorithm is implemented in Landlab, see *Adams et al.* [2017].

3.1.3 Depth-dependent Manning's roughness

To resolve both hillslopes and channels within the model domain, a spatially and temporally variable Manning's roughness coefficient (n) was used to adjust calculated discharge. At each time step, Manning's n is calculated as a function of surface water depths [*Jain et al.*, 2004; *Jain and Singh*, 2005; *Mügler et al.*, 2011; *Rengers et al.*, 2016]. If surface water depth at a given node, calculated by the OverlandFlow component, falls beneath a threshold water depth, the roughness coefficient is recalculated for that location. All simulations shown in this work have a threshold water depth of 5 cm, as roughness values increase when water depths are shallower than 5 cm. Manning's n values are calculated using the logical statement:

$$n = \begin{cases} n_{min}(h/h_0)^{-\epsilon} & \text{if } h \leq h_0 \\ n_{min} & \text{if } h > h_0 \end{cases} \tag{7}$$

where n_{min} is the minimum roughness value for a given landscape $[L^{-1/3}T]$; h is the surface water depth $[L]$, h_0 is the threshold flow depth $[L]$ and ϵ is an exponent that describes drag related to vegetation. Spatially variable roughness (n) drives changes in surface water discharge (Eq. 5).

3.1.4 Detachment-limited erosion

To erode the landscape with nonsteady discharge, the Landlab DepthSlopeProductErosion component is used. This component calculates erosion rates and evolves the topography. Fluvial erosion rates are solved as a function of shear stress, and no deposition is considered. Following previous work [e.g. *Howard*, 1994; *Tucker*, 2004; *Lague et al.*, 2005], erosion rates are calculated as:

$$E = k_e(\tau^a - \tau_c^a) \tag{8}$$

where E is the erosion rate $[LT^{-1}]$; k_e is the erodibility coefficient, the units of which depend on the dimensionless positive exponent a; τ is the bed shear stress $[Pa]$; and τ_c is the critical shear stress threshold, below which no erosion occurs $[Pa]$. At each time step, shear stress on the channel bed (τ) is calculated using the depth-slope product:

$$\tau = \rho g h S_w \tag{9}$$

224 where ρ is the fluid density $[ML^{-3}]$; g is the gravitational acceleration $[LT^{-2}]$; h is the
225 surface water depth $[L]$ and S_w is the dimensionless surface water slope. Both water depth
226 and surface water slope values are calculated in the OverlandFlow component, and shared
227 with the DepthSlopeProductErosion component at each time step.

3.1.5 Linear hillslope diffusion

229 As first recognized by *Culling* [1960], linear diffusion is a good approximation for slow
230 erosive processes such as creep, bioturbation and rainsplash. In many landscape evolution
231 models, linear diffusion is used to generate convex hillslopes [e.g. *Willgoose et al.*, 1991;
232 *Tucker and Slingerland*, 1994; *Tucker and Bras*, 2000]. Diffusive processes are solved as:

$$q_s = -k_d \frac{\Delta z}{\Delta x} \tag{10}$$

233 where Δz is the change in elevation between nodes $[L]$ and k_d is the diffusivity coeffi-
234 cient $[LT^{-1}]$. The change in the topographic surface through time, driven by fluvial erosion
235 (E) and hillslope diffusion (q_s) as they compete with uplift (U) is calculated as:

$$\frac{\Delta z}{\Delta t} = U - (E + \frac{\Delta q_s}{\Delta x}). \tag{11}$$

3.1.6 Steady discharge and erosion

237 Most landscape evolution models assume surface water discharge is a single, tempo-
238 rally constant rate for a given storm, calculated as:

$$Q_{ss} = PA \tag{12}$$

239 where the discharge (Q_{ss}) is the product of rainfall intensity P and drainage area A
240 $[L^2]$. This steady discharge value drives erosion using the equation [e.g. *Attal et al.*, 2011]:

$$E_{ss} = k_s(\rho g n_{min}^{3/5} Q_{ss}^{0.5 m_{sp}} S_w^{n_{sp}} - \tau_c)^a \tag{13}$$

241 where E_{ss} is the erosion rate calculated using the steady discharge method $[LT^{-1}]$; k_s
242 is the erodibility constant, the units of which depend on the exponent m_{sp}; Q_{ss} surface water
243 discharge $[L^3 T^{-1}]$; S_w is surface water slope, estimated using the topographic slope; m_{sp} and
244 n_{sp} are dimensionless exponents on discharge and slope, respectively; and τ_c is the threshold
245 parameter, below which no erosion occurs $[Pa]$.

3.2 Experimental set-up

3.2.1 Incorporating rainfall variability

248 To capture climate variability, a rainfall variability metric, (R_{var}), was used, following
249 *Tucker and Bras* [2000] and *Istanbulluoglu and Bras* [2006]:

$$R_{var} = \frac{\overline{t_r} + \overline{t_b}}{\overline{t_r}} \tag{14}$$

250 where mean storm duration ($\overline{t_r}$) and mean interstorm duration ($\overline{t_b}$) are the same values
251 used in Eqs. (1) and (2). Large R_{var} values are found in locations characterized by shorter-
252 duration, higher-intensity rainfall events, while lower R_{var} values are found in wetter loca-
253 tions with 'drizzle-like' storms [*Istanbulluoglu and Bras*, 2006].

254 Figure 3 shows R_{var} values for several sampling sites throughout the United States,
255 determined using data from *Hawk* [1992]. To directly compare the impact of different R_{var}

values, sites with similar mean annual precipitation depths were used to parameterize the stochastic storm generator. This experimental design is similar to *Tucker and Bras* [2000], but considers a greater range of R_{var} values. The characteristics of the two variability cases are outlined in Table (3). Figure 4 illustrates the generated 1,000 year time series of storm duration, depth and intensity for both R_{var} values. The differences between the two variability cases are clear in this figure: generally, storms in the lower R_{var} case have longer durations, while storms in the higher R_{var} case have greater intensities and depths. Due to constraints in the nonsteady discharge component, very low intensities had to be removed from the time series, as the model becomes unstable when routing extremely shallow water depths. That lower intensity threshold for all model runs was set as 0.5 mm hr^{-1}.

The sampled low and high R_{var} cases are contrasted directly in Fig. (5). The histograms illustrate that, even considering the removal of low intensity storms (P $\leq$ 0.5 mm hr $^{-1}$), the probability of a low intensity ($\leq$ 1 mm hr^{-1}, Fig. 5a) or low depth ($\leq$ 5 mm hr^{-1}, Fig. 5a) event occurring is much greater in the low R_{var} case than an event of similar intensity in the high R_{var} case (Fig. 5a, c). The probability of larger intensities and depths in the high R_{var} case are clearly illustrated in Figs. (5b, d). Note that any differences between the modeled climates are likely underestimated because of the need to remove the smallest storms, which occur more frequently in the low R_{var} case.

3.2.2 Landscape evolution runs with nonsteady discharge

Sampled storm time series for both rainfall variability test cases were used to drive overland flow across the landscape and evolve the model topography. All storm events were spatially uniform across the entire domain and had a temporally constant intensity (P) for a given storm duration (t_r). To directly compare erosion results from the two variability time series, we opted to run the simulations until 20 m of rainfall was routed across the landscape. The thick vertical lines in Fig. (4) indicate the number of events it takes to reach a given total rainfall depth for each R_{var} case. For this sampled series of events, the high R_{var} case reaches 20 m of input rainfall several hundred events before the low R_{var} case. Because erosion occurs as a function of water depth (Eq. 9), we chose to compare the landscapes after an equal depth of water was routed in each case, albeit in different configurations. In all nonsteady cases, the exponent a in Eq. (8) was set to 1. After each individual storm event, the landscape was uplifted and diffused (Eq. 11) for the storm duration and interstorm duration of each event ($t_r + t_b$).

Due to variability in water depths and water surface slopes near the grid outlet, pits can form which prevent the flood hydrograph from exiting the domain. This occurs when erosion is happening at a faster pace than uplift. The erodibility constant k_e was tuned to prevent the creation and propagation of these pits. k_e was calibrated using the largest storm depth occurring during the 20 m rainfall window, as this event would have the greatest overall erosion nearest the outlet. This event occurred during the high R_{var} time series (Fig. 4b).

For each storm variability scenario, the critical shear stress threshold τ_c was systematically changed to simulate a range of entrainment conditions (asterisked values in Table 4). Previous work using this modeling setup showed negligible impact of changing parameter a [*Adams*, 2017]. In total, 4 nonsteady runs were completed for each climate case.

3.2.3 Traditional landscape evolution runs with steady discharge

Similar to the nonsteady discharge runs, sampled storm time series for the two climate variabilities (Fig. 4) were used to calculate steady discharge (Eq. 12) and erosion rates (Eq. 13). Figure 6 illustrates the difference between the two discharge methods: in both methods, the volume of water is the same but the distribution of flow through time changes. For each climate time series, the same rainfall time series, up to 20 m depths, were routed across the domain. In the steady discharge method, discharge rates are temporally constant throughout

305 a storm event, and discharge ceases when the storm event ends (e.g. Q_{ss} in Fig. 6). Storms
306 were modeled as spatially uniform. Following each individual storm event, the landscape
307 was uplifted and diffused (Eq. 11) for the storm duration and interstorm duration of each
308 event ($t_r + t_b$).

309   To calculate erosion, the erodibility parameter k_s was tuned to the approximate erosion
310 magnitudes seen at the outlet in the nonsteady case for the largest storm event (Fig. 4b). In
311 all steady discharge and erosion model runs, the exponent a was set to 1. For both climate
312 variability cases, erosion depths and patterns were compared to the nonsteady discharge re-
313 sults. The steady discharge model runs were less sensitive to τ_c, so a larger range of τ_c val-
314 ues was tested to explore differences between the two climate types and discharge conditions
315 (Table 4).

4 Results

4.1 Nonsteady discharge and storm characteristics

318   For all runs, total eroded depths were saved across the model domain. Time series of
319 changing erosion rates were output for each of the seven locations indicated in Fig. (1). Me-
320 dian erosion rates and discharges were calculated at these sampling locations for each storm
321 event. Median values are calculated as the median of all discrete, nonzero erosion rates or
322 discharges occurring during a given storm and subsequent interstorm duration. Erosion rates
323 and patterns are highly sensitive to changes in storm duration, intensity and critical shear
324 stress threshold. For each location, the correlation coefficient between event median erosion
325 rate and storm characteristics (duration and intensity) was calculated for each critical shear
326 stress value ($0 \leq \tau_c \leq 10$ Pa, Fig. 7). When τ_c is low, the median erosion rates are more
327 strongly correlated with storm duration at all sampled locations. Without a threshold, or with
328 a minimal threshold limiting erosion, the duration of surface water flow has the largest im-
329 pact on erosion (Fig. 7a, b). The correlation coefficients between median erosion rate and
330 storm duration slightly decreases with increasing critical shear stress because more water
331 (greater intensity) is needed to surpass the threshold for incision.

332   The correlation coefficients for the median erosion rate and storm intensity data illus-
333 trate a reversed pattern from those between median erosion rate and storm duration (Fig. 7c,
334 d). Median erosion rates are more weakly correlated with intensity than storm duration re-
335 gardless of the τ_c value or location in the watershed. As τ_c increases, erosion rates becomes
336 more moderately correlated with intensity. This suggests that as τ_c increases, erosion rates
337 become less dependent on the duration of water on the surface of the domain, and more de-
338 pendent on higher intensities to surpass the critical shear stress threshold.

339   The upstream sensitivity to storm parameters can also be illustrated by comparing the
340 median erosion rate and median discharge value, where the median discharge is calculated as
341 the median value of all discrete discharge values occurring throughout an event hydrograph.
342 Figure 8 shows the relationship between these data for both climate variability cases. When
343 $\tau_c = 0$, there is clear relationship between median erosion rate and median discharge at all
344 sampling locations (Fig. 8a-c). As critical shear stress increases, more scatter is introduced
345 into the trend. In particular, when median discharge is lower, erosion rates are more sensitive
346 to critical shear stress and erosion is reduced (e.g. Fig. 8d). These patterns and deviation
347 from the linear trend are most apparent in the upstream locations of the domain, although
348 some scatter is evident in the midstream and outlet locations (Fig. 8e,f).

4.2 Erosive imprint of rainfall variability with nonsteady discharge

350   Spatial fluvial erosion patterns from the nonsteady discharge cases are comparable for
351 each of the two rainfall time series. Figure 9 shows that erosion depths after 20 m of rain-
352 fall, log-binned and averaged by area, increase moving downstream. For a given drainage

353 area, erosion depths decrease with increasing incision threshold τ_c, with more significant de-
354 creases occurring upstream. For both rainfall variability cases, there is a notable decrease in
355 erosion rates when τ_c increases from 5 Pa to 10 Pa, with a slightly larger decrease in the low
356 R_{var} case (Fig. 9a), caused by the inability of some lower intensity storms to erode above the
357 given τ_c threshold.

358 Comparing the low R_{var} (Fig. 9a) and high R_{var} (Fig. 9b) erosion results for a given
359 value of τ_c illustrates the sensitivity of each case to the critical shear stress threshold. When
360 no critical shear stress is considered, the low variability case has greater overall erosion (Fig.
361 9c). This suggests that the greater number of low intensity storms have a larger cumulative
362 erosive impact than a smaller number of high intensity storms in the highly variable climate.
363 As τ_c increases to 1 Pa, the two climate cases have similar eroded depths, although the lower
364 variability case still has slightly greater erosive power (Fig. 9d). However, small changes in
365 critical shear stress can have a significant impact on erosion patterns, as seen when τ_c is 10
366 Pa or higher. In these cases, erosion results for the rainfall variabilities switch, particularly
367 in the upland portion of the catchment, where the higher rainfall intensities of the high R_{var}
368 case drive more cumulative erosion than the smaller intensity storms in the low R_{var} case
369 (Fig. 9e,f).

4.3 Comparison to steady discharge method

371 The steady discharge erosion patterns differ from those using the nonsteady method.
372 In particular, erosion results from the steady discharge are spatially uniform in the channel-
373 ized portion of the domain (Fig. 10). These patterns are the same in both the low and high
374 R_{var} cases, despite the differences in discharge between the storm events. With an increase
375 in τ_c, there is a small decrease in eroded depths, as seen in the nonsteady discharge runs. The
376 steady discharge model was less sensitive to the τ_c values used in the nonsteady case and so
377 a larger range of τ_c values was tested (Table 4). Even when τ_c reaches 50 Pa, there is only
378 a very small decrease in erosion depths, with a similar drops seen in both the high R_{var} and
379 low R_{var} cases (Fig. 10). Erosion depth results for the two rainfall variabilities are also com-
380 pared directly for a given τ_c value. In all τ_c cases, the low R_{var} storm series drives higher
381 overall erosion compared to the high R_{var} case.

382 To explore the differences between the steady and nonsteady discharge methods, ero-
383 sion depths were normalized to the outlet erosion depth value for each rainfall variability test
384 case (Fig. 11). Because the initial landscape had reached steady-state, most of the fluvially
385 eroded depths from the steady discharge model fall along the line of unity, except for the
386 hillslopes, which fall beneath that line. When normalized, the erosion results in the steady
387 discharge model for the two rainfall variabilities overlap, demonstrating the method creates
388 identical spatial patterns regardless of storm series used to drive erosion (Fig. 11, gray sym-
389 bols). For the nonsteady discharge case, all values upstream of the outlet fall beneath the line
390 of unity (Fig. 11, black symbols). When $\tau_c = 0$ Pa, the upstream pattern in eroded depths in
391 the low R_{var} case is the same as the pattern in the high R_{var} case (Fig. 11a). As τ_c increases
392 to 10 Pa, there is a greater upstream reduction in total eroded depths in the low R_{var} case
393 relative to the high R_{var} case (Fig. 11b).

394 While it is difficult to directly relate the absolute values of erosion depths predicted by
395 steady and nonsteady methods, it is valuable to explore the fundamental difference between
396 the two sets of experiments: how they calculate surface water discharge. The probability dis-
397 tributions of surface water discharge for the two discharge methods are shown in Fig. (12a).
398 For a given discharge method, the low R_{var} case has a greater probability of lower discharge
399 values. The high R_{var} case has an increased likelihood of larger discharge events relative
400 to the low R_{var} case. The steady discharge method consistently produces greater discharge
401 values than the nonsteady method, and greater discharge values produce greater overall ero-
402 sion depths. This pattern is apparent when plotting the modeled steady discharge against the
403 median nonsteady discharge. For a given discharge event, the steady discharge rate exceeds

the median value of the nonsteady method (Fig. 12). These patterns occur at both the outlet (Fig. 12b) and upstream-most sampling location (Fig. 12c). When the values plot along the 1:1 line, that indicates that a storm duration occurred long enough for the nonsteady method to reach time to concentration of a given storm intensity, and that the hydrograph reached the steady discharge value for the majority of the overland flow event (e.g. example hydrographs in Fig. 6). During these long duration events, the median discharge value falls along the long, flat top of the hydrographs. In the upstream location, no median values from the nonsteady method ever reach the predicted steady value, likely due to the steepness of the terrain. If the water drains quickly from a given cell, flow cannot collect and reach the higher discharge values that are seen in the steady method.

5 Discussion: Hydrologic variability and the implications for landscape form

Previous studies have explored the concept of geomorphic work and how it is controlled by climatic variability. Most studies that address the impact of climate variability on erosion have considered steady discharge or single discharge values, some with the added complexity of stochastic storms and/or erosion thresholds [*Tucker and Bras*, 2000; *Snyder et al.*, 2003; *Tucker*, 2004; *Lague et al.*, 2005; *Istanbulluoglu and Bras*, 2006; *DiBiase and Whipple*, 2011; *Sorensen and Yanites*, 2019]. This study adds a new level of complexity, by exploring the interaction of rainfall variability and fluvial erosion driven by a nonsteady discharge model. By including hydrograph dynamics, we are able to fully couple rainfall and overland flow variability within a geomorphic model and examine the impacts of hydrologic variability on erosion rates, patterns and landscape form.

Following the existing literature on hydrograph dynamics, results from the nonsteady discharge case are sensitive to the storm characteristics of duration and intensity [e.g. *Snyder*, 1938; *Black*, 1972; *Ogden and Julien*, 1993; *Adams et al.*, 2017]. This sensitivity is translated to the erosion results, as the dynamics of a flood wave can cause spatial variations in erosion depths on a highly localized scale. However, the correlation between erosion and rainfall characteristics is not uniform across the model domain. In particular, erosion rates and depths in smaller drainage areas are more sensitive to changes in storm parameters and τ_c (e.g. Figs. 7, 9). The correlation between erosion rates with storm duration is tied to the period of time the flood wave is occurring at a given location.

Hydrographs generated in upstream locations are often shorter in duration than hydrographs in higher drainage areas. In particular, the duration of an upstream hydrograph may more closely approximate the given storm duration, whereas the outlet hydrograph can last much longer than the storm. When the critical shear stress is zero, erosion occurs throughout the entire event hydrograph and erosion rates are more strongly correlated with storm duration. However, erosion rates at locations with small drainage areas become more strongly correlated with storm intensity as τ_c is increased, as the erosive power of the flood has to surpass higher shear stress values to initiate erosion. Like the nonsteady discharge case, erosion rates driven by steady discharge would also be tied to the intensity and τ_c value, because of the intensity parameter in Eq. (12). However, the erosion rate in the steady discharge case will have no correlation with storm duration, as the erosion rate is steady throughout a storm event.

The sensitivity of discharge and erosion results to precipitation parameters conform to results from previous work. *Nearing et al.* [2005] used seven event-based distributed soil erosion models to simulate runoff-driven erosion, and consider changes in erosion with systematic changes in rainfall intensity and depths. Their work demonstrated that erosion was sensitive to changes in both rainfall intensity and volume, with increases in either rainfall parameter driving an increase in erosion. Similar results have been shown in field studies of agricultural erosion [*Arnaez et al.*, 2007] and numerical modeling studies of gully initiation and erosion [*Hoober et al.*, 2017].

The erosion depth results presented in this study also respond to changes in the critical shear stress value. As shown by *Tucker* [2004], topographies modeled with stochastic rainfall and steady discharge were affected by the inclusion of a critical shear stress, with greater relief in higher τ_c cases. Theoretical studies using a discharge threshold [*Lague et al.*, 2005; *Molnar et al.*, 2006; *DiBiase and Whipple*, 2011] show similar sensitivities. With the inclusion of variable rainfall, erosion rates will either increase or decrease depending on an erosion threshold and the nonlinearity of the erosion equation [*Tucker and Bras*, 2000; *Tucker*, 2004; *Lague et al.*, 2005; *Molnar et al.*, 2006; *DiBiase and Whipple*, 2011]. These patterns are seen in both the nonsteady (Fig. 9) and steady (Fig. 10) discharge cases presented here. In both discharge methods, determining which climate scenario is the most erosive is dependent on the τ_c value prescribed in the model. In both overland flow methods, the low R_{var} case has greater erosive power when τ_c is low. As τ_c is increased, the larger floods of the high R_{var} case will drive greater overall erosion, especially in lowest drainage ares and hillslopes. The storm series in Fig. (4) suggest that if we had run the model for longer, including more storm events, the erosion gap between the high and low variability cases would widen due to the more intense events in the high R_{var} case. This gap in erosion depths would be exacerbated further if the low intensity storms that were sampled out (P $\leq$ 0.5 mm hr^{-1}) were included, as these small events could dampen overall erosion depths in the low R_{var} case, particularly if nonzero τ_c values are considered. Overall, determining which climate variability or flood distribution does more erosive work will be determined by characteristics such as the grain size distribution of a particular location.

The key distinction between this study and previous work is including the additional complexity of modeling overland flow. Previous work exploring erosion driven by rainfall variability calculated erosion as a function of steady discharge, whereas this work uses an explicit solution of the shallow water equations to generate hydrographs across the modeled terrain. The trends of erosion magnitudes in the steady discharge method follow those in the nonsteady method, with a decrease in overall eroded depths as a function of τ_c (Fig. 10). Steady discharge methods predict spatially uniform erosion depths in the channelized region of the domain (Fig. 10), suggesting unchanging concavity and relief.

To compare the steady and nonsteady discharge erosion results directly, each test case was normalized to the outlet eroded depth (Fig. 11). Normalized erosion depths from the steady discharge method are relatively comparable across the basin, falling within a range of an order of magnitude or less. Erosion patterns from the steady discharge model runs suggest that the morphology of the landscape would not change much if modeled with a stochastic storm generator.

In contrast to the steady discharge model results, erosion patterns from the nonsteady discharge case demonstrate a more complex response, with a notable downstream increase in erosion depths, which span several orders of magnitude (Fig. 11). This would produce landscapes distinct from those in the steady discharge method, with increased channel concavities as upstream locations steepen to match the downstream erosion rates [*Adams et al.*, 2017]. The stark contrast between erosion depths and patterns in the steady and nonsteady discharge runs can be explained by the different ways they handle discharge (Fig. 12). Models assuming steady discharge assume a maximum flood discharge for the duration of a storm event, potentially overestimating erosive power at all locations in the grid. This is illustrated in Fig. (12, dashed lines), where the steady discharge method produces large discharge relative to the median discharge produced by the nonsteady method (Fig. 12, solid lines). Because hydrographs capture a range of discharges and erosion rates, the median values of both may be much less than the steady discharge method. These patterns are seen at the outlet sampling site (Fig. 12b) and in the upstream reaches of a watershed (Fig. 12c). Due to these fundamental differences in discharge patterns, and therefore erosion patterns, it is clear that modeled landscape form depends on the discharge method used. For example, landscapes evolved with nonsteady discharge conditions are likely to have greater channel concavities than landscapes evolved using the steady discharge model, as the upstream portion of the landscape

507 would need to steepen to reach conditions where erosion rates are uniform across the do-
508 main.

6 Summary and conclusions

510   Using a model that combines stochastic storms, overland flow generation and fluvial
511 incision, this work explores the imprint of discharge variability on landscape form. Two rain-
512 fall time series, representing high and low variability endmember cases, were used to initiate
513 steady and nonsteady discharge. Results demonstrate that the nonsteady discharge method is
514 sensitive to differences in precipitation characteristics across the two climate regimes. This
515 sensitivity is captured in the erosion results, with increasing erosion depths moving from up-
516 stream to downstream, patterns that can be amplified or reduced with the changes to the crit-
517 ical shear stress value applied in the model. However, the correlation between erosion rates
518 and precipitation characteristics is not uniform across the domain, as locations with smaller
519 drainage areas are more sensitive to changes in duration and intensity than locations down-
520 stream.

521   Erosion rates calculated using the steady discharge method are sensitive to changes
522 in storm intensity, but the imprint of storm duration is not captured. The steady discharge
523 model runs illustrate that erosion depths do not vary systematically in space, suggesting that
524 the introduction of stochastic storms is not enough to shift a landscape out of steady-state
525 and into transience. Similar to the nonsteady discharge method, these erosion results are also
526 sensitive to the prescribed critical shear stress value, although to a much smaller degree.

527   Overall, the sensitivity of erosion results to discharge method suggests that the inte-
528 grated erosive impact of a hydrograph cannot be ignored as a potential driver of landscape
529 form. The geomorphic effectiveness of a given climate variability, or which R_{var} case drives
530 higher erosion, is dependent on the erosion threshold applied in the model. When critical
531 shear stresses are low, less variable climates are capable of more erosive work. As the criti-
532 cal shear stress value is increased, highly variable climates can become more geomorphically
533 effective, as higher intensity storms are required to initiate erosion throughout the domain.
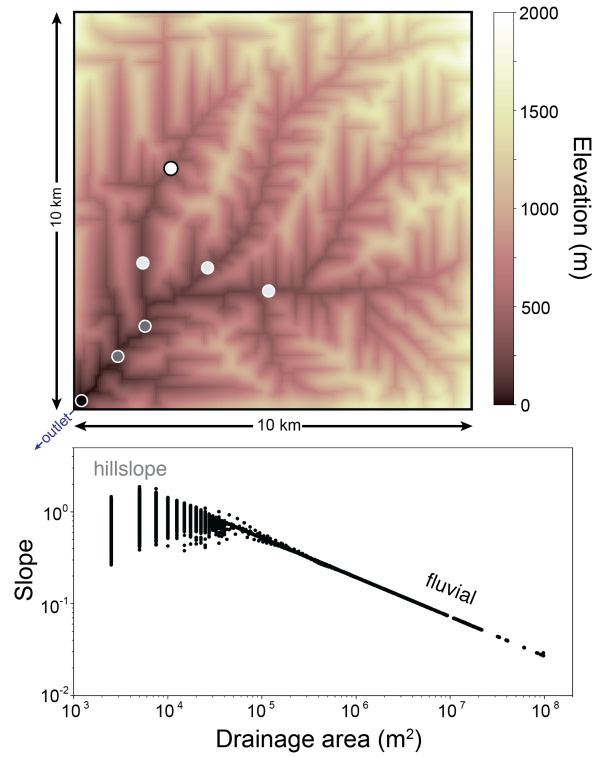
Figure 1. Synthetic 100 km^2 topography used in all model runs. The test basin was evolved to topographic steady state using steady D4 flow routing, fluvial erosion and hillslope diffusion components in Landlab. All flow exits the test basin in the southwest corner at an open boundary node. All other perimeter nodes are set as closed boundaries. Seven sampling locations across the domain are shown. These sampling sites are grouped as follows: one upstream site (white, drainage area of 10^7 m^2); three midstream sites (light gray, average drainage area of $2.3 \cdot 10^7$ m^2); two downstream sites (dark gray, average drainage area of $8.8 \cdot 10^7$ m^2) and the watershed outlet (black, drainage area 10^8 m^2). The process zones for the model domain are indicated in the slope-area data.
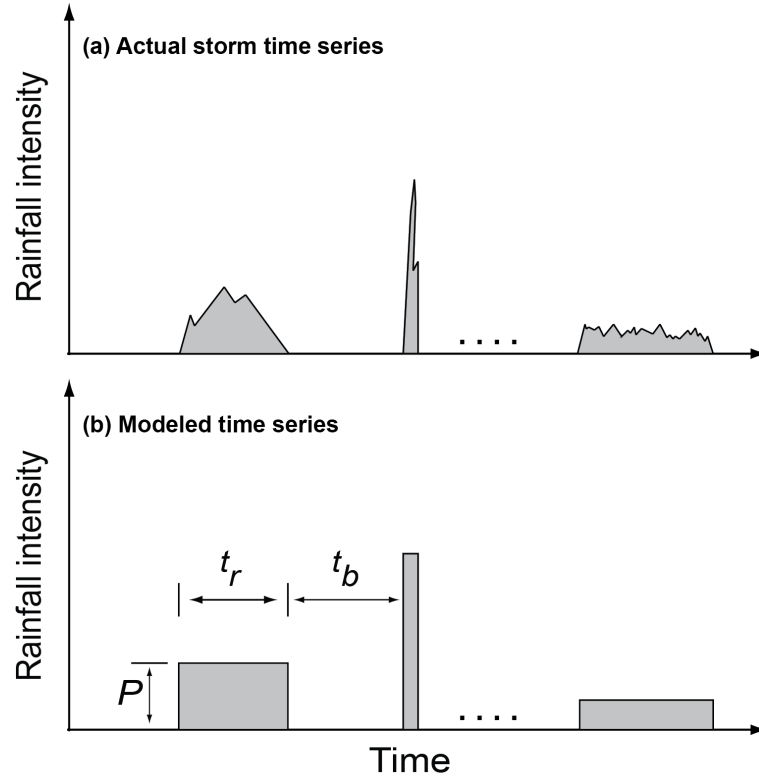
Figure 2. Adapted from *Tucker and Bras* [2000], this diagram compares (**a**) a hypothetical 'natural' rainfall time series and (**b**) the same time series generated by the rectangular pulse Poisson rainfall model. In the hypothetical time series, rainfall intensity (P) may vary within a given storm duration (t_r). In the modeled time series, rainfall intensity is considered temporally constant for the duration of a storm event. Some interstorm duration (t_b) separates the storm events.
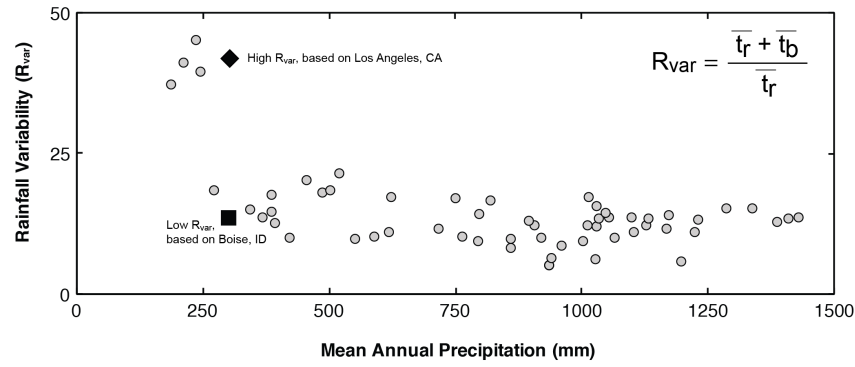
Figure 3. Adapted from *Istanbulluoglu and Bras* [2006], this figure illustrates the relationship between rainfall variability (R_{var}) and mean annual precipitation for several locations. Two sampling locations with similar mean annual precipitation, but different R_{var} values are highlighted: a high R_{var} site (parameterized using data from Los Angeles, CA) is denoted with a black diamond; a low R_{var} site (parameterized using data from Boise, ID) is marked with a black square. Data for this plot were drawn from *Hawk* [1992].
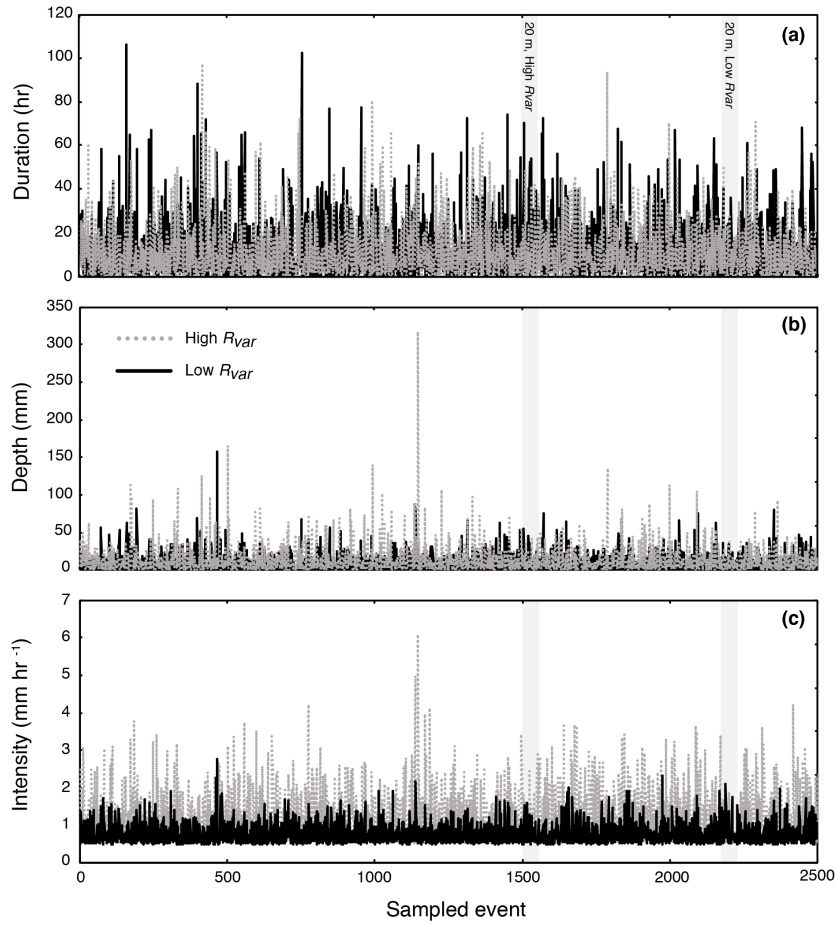
Figure 4. Comparison of the sampled duration (**a**), depth (**b**) and intensity (**c**) events for both the high and low variability datasets. Vertical gray lines indicate the number of events it takes to reach a total rainfall depth of 20 m rainfall depth for both climate scenarios. Note that for the lower rainfall variability dataset, it takes a larger number of events to reach those depths. For clarity, high R_{var} data are plotted above low R_{var} data in panels **a** and **b**, while the low R_{var} data are plotted on top in panel **c**.
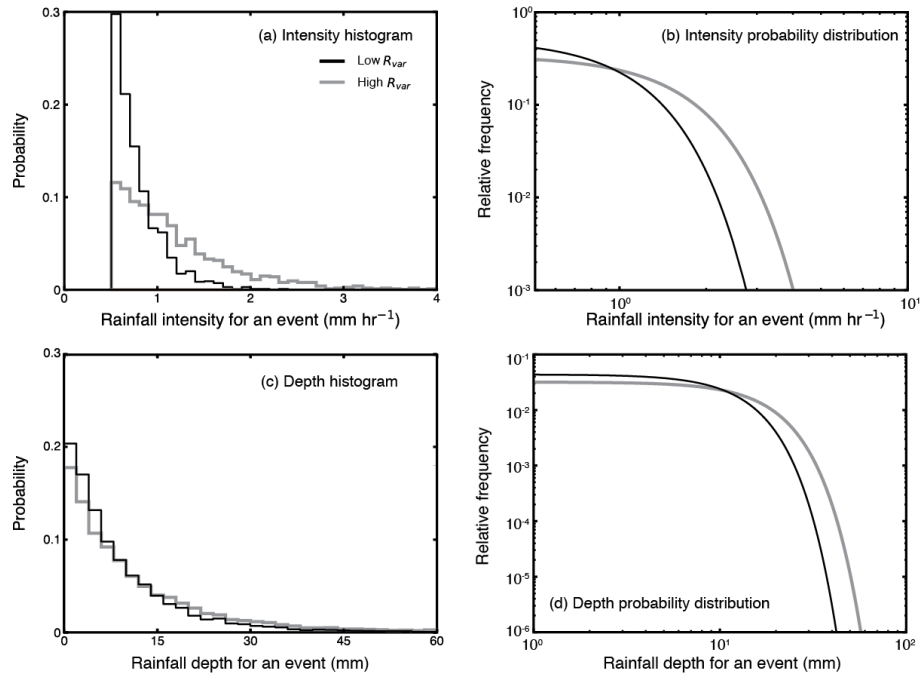
Figure 5. Comparison of probability distributions for the sampled high and low variability datasets. Panel (**a**) compares the sampled intensity histograms for both of the climate variabilities, panel (**b**) shows the log-transformed exceedance frequency plot for a given intensity. Panels (**c**-**d**) illustrate the same statistics for rainfall depth.
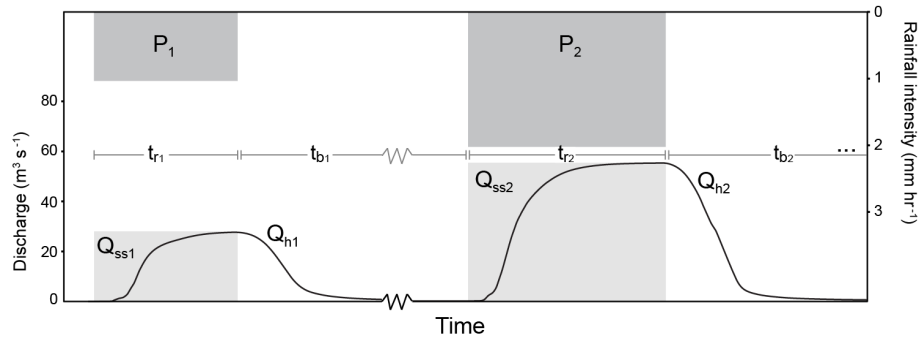
Figure 6. Modeled output illustrating the two flow routing approaches of this study. In response to the stochastic storm generator, the OverlandFlow method has a prolonged hydrograph (Q_h) compared to the traditional steady discharge method (Q_{ss}), which only generates a discharge value for the duration of a given storm event (t_r).
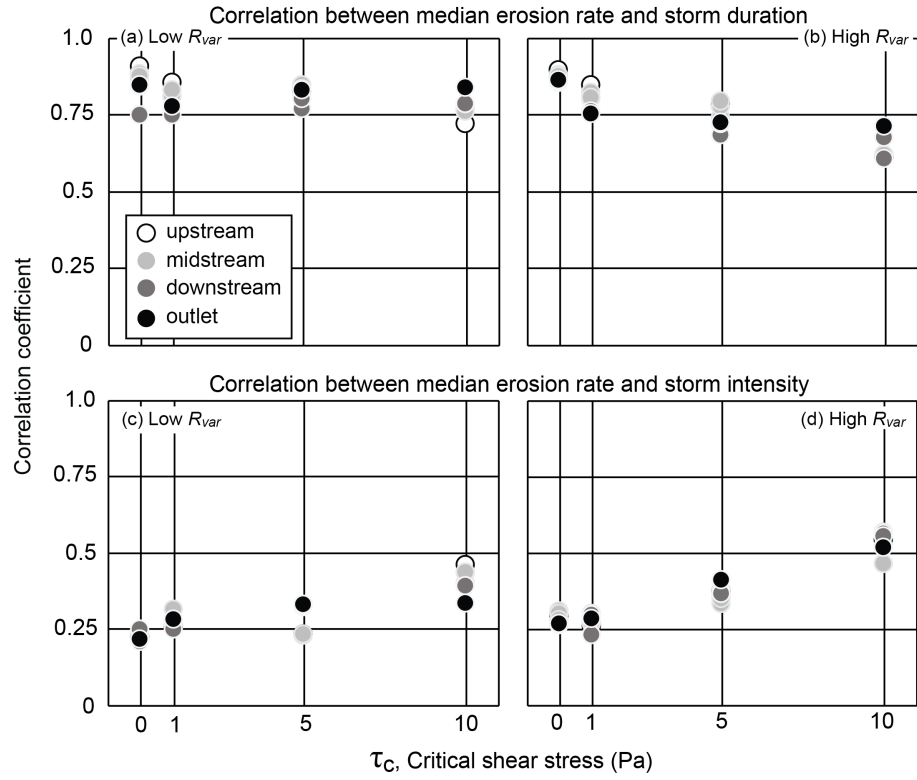
Figure 7. Correlation coefficients for erosion rates and storm characteristics from seven sampling locations throughout the domain (Fig. 1). Panels (**a-b**) show the correlation between erosion rate and storm duration with increasing τ_c for both variability cases. Panels (**c-d**) illustrate the correlation between erosion rate and storm intensity with increasing τ_c for both variability cases.
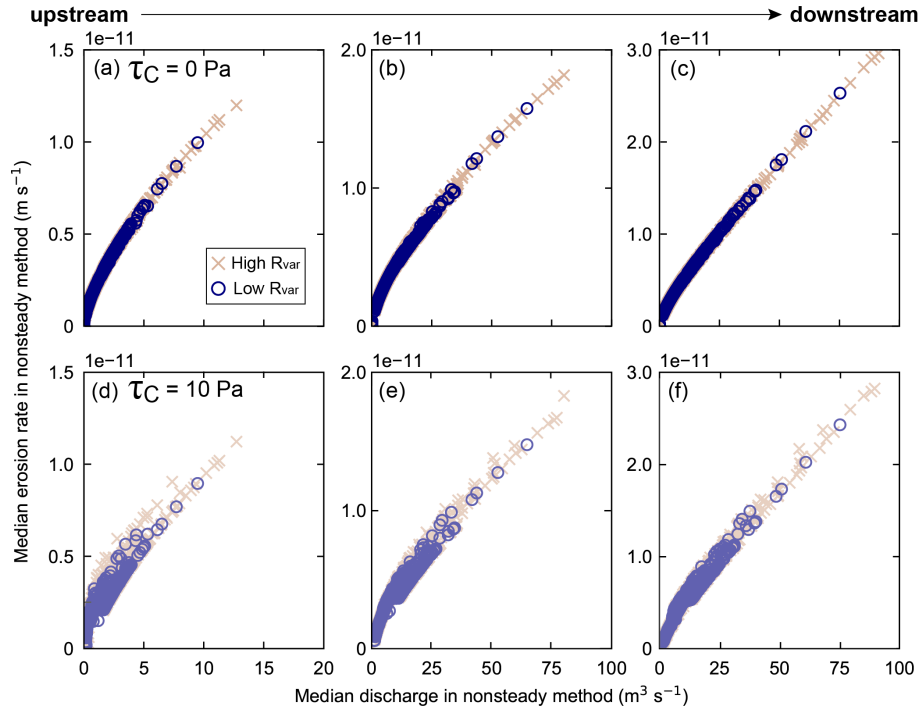
Figure 8. The relationship between the median erosion rate and nonsteady median discharge when $\tau_c = 0$ Pa (panels **a-c**) and $\tau_c = 10$ Pa (panels **d-f**). Each data point represents an individual storm event. Data are plotted for the upstream (**a, d**), midstream (**b, e**) and outlet (**c, f**) sampling locations.
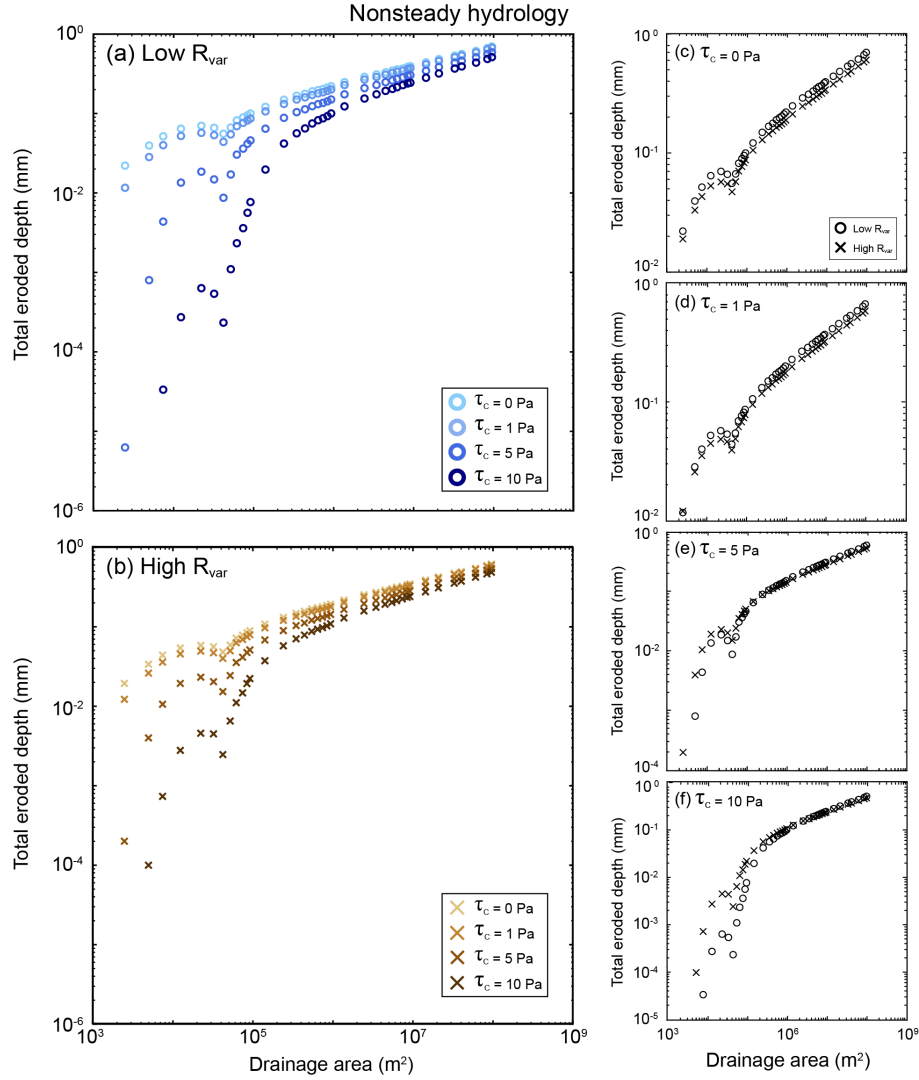
Figure 9. Fluvially-eroded depths, log-binned and averaged by area, across the domain generated using nonsteady discharge for the low R_{var} (**a**) and high R_{var} (**b**) cases. Different colors in panels (**a-b**) indicate different τ_c values. Panels (**c-f**) compare total eroded depths for each climate variability and τ_c. Note that panels (**c-f**) have different axes.
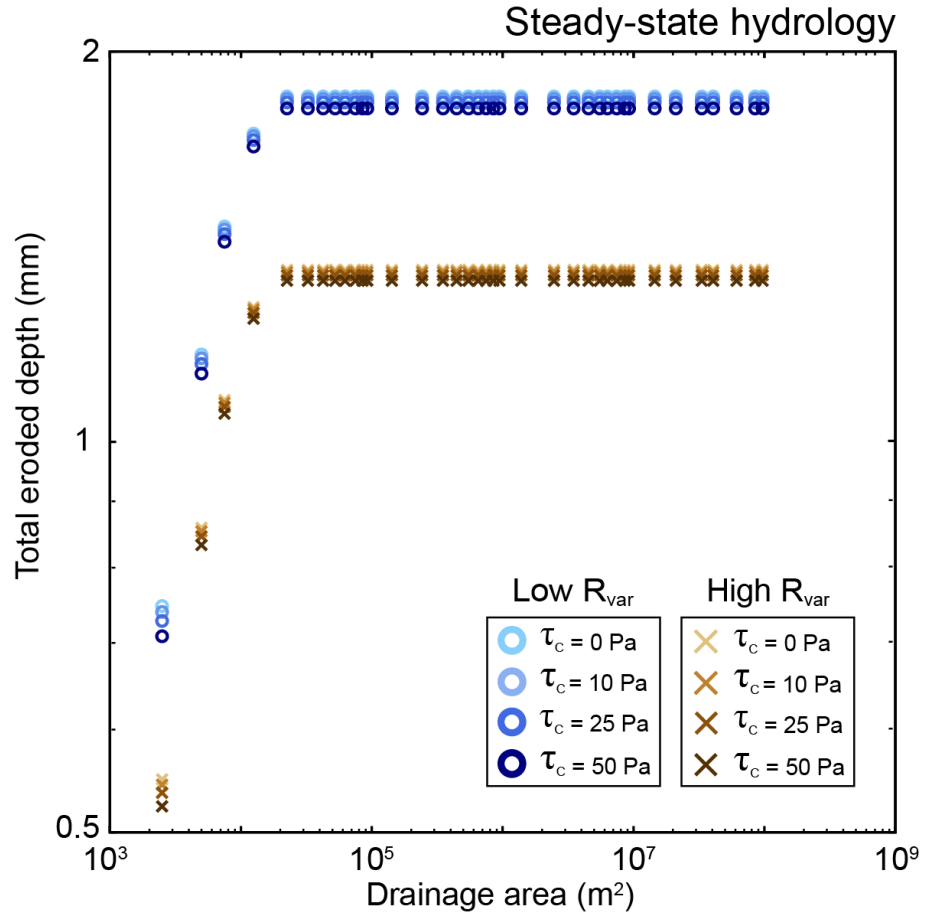
Figure 10. Fluvially-eroded depths, log-binned and averaged by area, across the domain generated using steady discharge for the low R_{var} and high R_{var} cases.
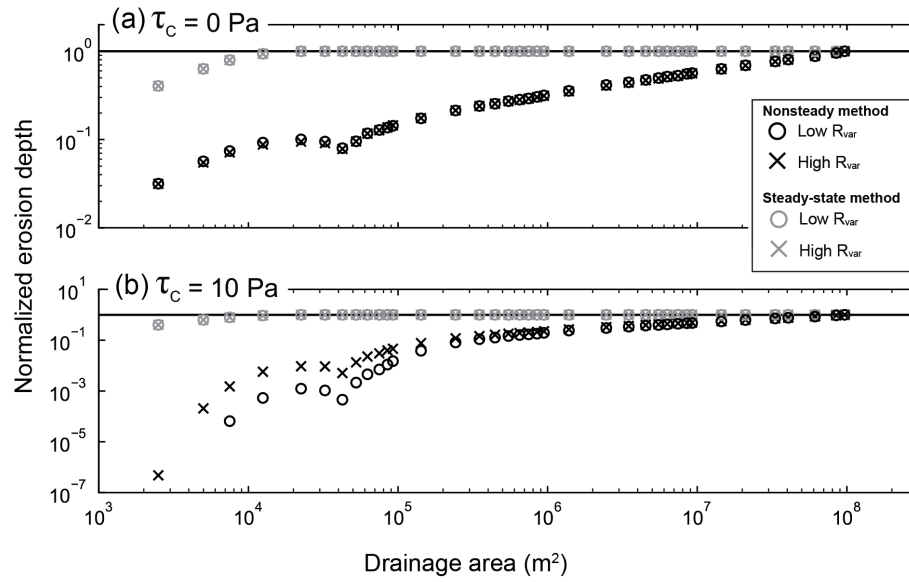
Figure 11. Normalized erosion rates for both climate regimes, generated using the steady (gray symbols) and nonsteady discharge methods (black symbols), when (**a**) τ_c = 0 Pa and (**b**) τ_c = 10 Pa. Data were normalized to the outlet erosion value for each specific case.
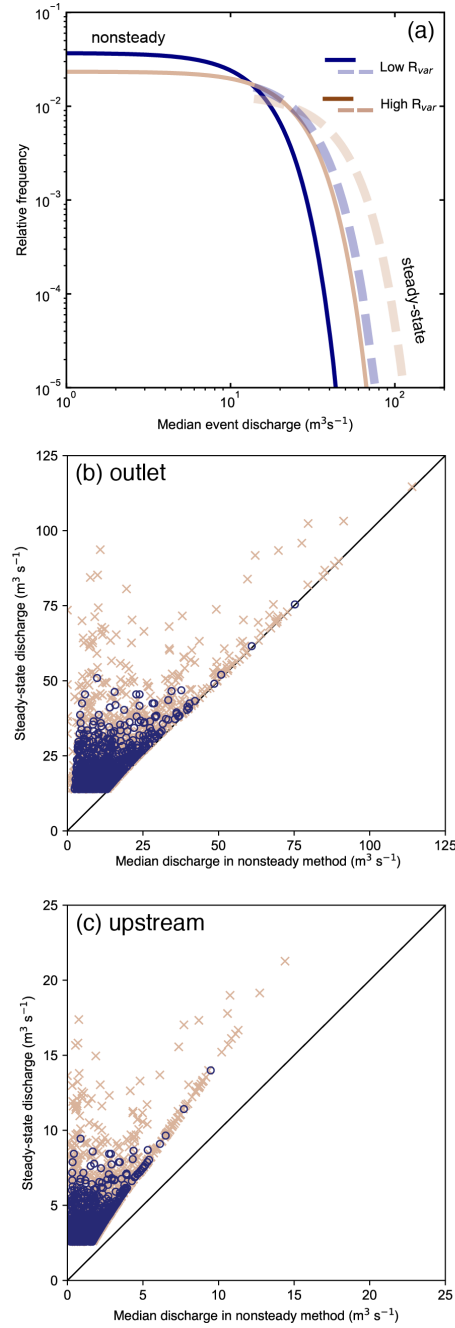
Figure 12. Panel (**a**) shows the relative frequency of the median event discharges for the two variability cases. Nonsteady data are plotted as solid lines; steady discharge data are dashed. Panels (**b-c**) compare steady discharge and nonsteady median discharge values for individual storms. The solid diagonal line indicates the 1:1 line. In most cases at the outlet (**b**) and all cases upstream (**c**), steady discharges exceed the nonsteady median value.

586

Table 1.   Variables in each model run.

Symbol	Name	Units
P	precipitation rate	$mm\ hr^{-1}$
t_r	storm duration	hr
t_b	interstorm duration	hr
d	rainfall depth	mm
h	surface water depth	m
q	surface water discharge per unit width	$m^2 s^{-1}$
S_w	surface water slope	–
n	Manning's roughness coefficient	$sm^{-1/3}$
Q_h	volumetric nonsteady water discharge	$m^3 s^{-1}$
E	incision rate calculated using non-steady discharge	ms^{-1}
τ	shear stress	Pa
Q_{ss}	volumetric steady water discharge	$m^3 s^{-1}$
E_{ss}	incision rate calculated using steady discharge	ms^{-1}
A	drainage area	m^2

587 **Table 2.** Model parameters for the overland flow, detachment-limited erosion and linear diffusion compo-
588 nents.

Symbol	Name	Value(s)	Units
Δx	grid resolution	50	m
$\overline{t_r}$	mean storm duration	Table 3	hr
$\overline{t_b}$	mean interstorm duration	Table 3	hr
$\overline{d}$	mean storm depth	Table 3	mm
Δt	time step	adaptive	s
α	time step stability coefficient	0.2	–
g	gravitational acceleration	9.81	ms^{-2}
θ	discharge weighting coefficient	0.8	–
n_{min}	minimum Manning's n	0.03	$sm^{-1/3}$
h_0	threshold flow depth	0.05	m
ϵ	drag exponent	1./3.	–
k_e	erodibility coefficient	$1. * 10^{-13}$	$m^{1+a}s^{2a-1}kg^{-a}$
τ_c *	shear stress threshold	Table 4	Pa
a	shear stress equation exponent	1.	–
ρ	density of water	1000.	$kg\ m^{-3}$
U	uplift rate	0.001	$m\ yr^{-1}$
k_d	diffusivity coefficient	0.1	$m^2 yr^{-1}$
k_s	steady discharge erodibility coefficient	$1. * 10^{-10}$	$m^{1-2m_{sP}}s^{-1}$
m_{sP}	steady incision equation exponent	0.6	–
n_{sP}	steady incision equation exponent	0.7	–

Note: not all values tested in both discharge cases

589 **Table 3.** Mean rainfall parameters for the stochastic Poisson rectangular pulse rainfall model. Average of the

590 12 monthly values reported by *Hawk* [1992]. Data for the high R_{var} case drawn from Los Angeles, CA data;

591 the low R_{var} case drawn from Boise, ID data.

Variability	Mean storm duration ($\overline{t_r}$, hr)	Mean interstorm duration ($\overline{t_b}$, hr)	Mean depth ($\overline{d}$, mm)
High R$_{var}$	10.75	433.58	9.62
Low R$_{var}$	11.75	146.25	4.775

592 **Table 4.** Critical shear stress values used in erosion runs. Grain sizes are approximate for a given τ_c, esti-
593 mated using data from *Julien* [2010].

Critical shear stress (τ_c)	Clast name	Maximum clast diameter
0*	-	-
1.0*	Sand	~1 mm
5.0*	Fine gravel	~6 mm
10.0*	Medium gravel	~12 mm
25.0	Very coarse gravel	~32 mm
50.0	Small cobbles	~64 mm

* Values tested in nonsteady discharge case.

References

Adams, J. M. (2017), Hydrograph generation and fluvial erosion: using landlab to explore how flood waves sculpt landscapes, Ph.D. thesis, Tulane University.

Adams, J. M., N. M. Gasparini, D. E. J. Hobley, G. E. Tucker, E. W. H. Hutton, S. S. Nudurupati, and E. Istanbulluoglu (2017), The landlab v1.0 overlandflow component: a python tool for computing shallow-water flow across watersheds, *Geoscientific Model Development*, *10*(4), 1645, doi:10.5194/gmd-10-1645-2017.

Arnaez, J., T. Lasanta, P. Ruiz-Flaño, and L. Ortigosa (2007), Factors affecting runoff and erosion under simulated rainfall in mediterranean vineyards, *Soil and Tillage Research*, *93*(2), 324–334, doi:10.1016/j.still.2006.05.013.

Attal, M., G. E. Tucker, A. C. Whittaker, P. A. Cowie, and G. P. Roberts (2008), Modeling fluvial incision and transient landscape evolution: Influence of dynamic channel adjustment, *Journal of Geophysical Research: Earth Surface*, *113*(F3), doi:10.1029/2007JF000893.

Attal, M., P. A. Cowie, A. C. Whittaker, D. E. J. Hobley, G. E. Tucker, and G. P. Roberts (2011), Testing fluvial erosion models using the transient response of bedrock rivers to tectonic forcing in the apennines, italy, *Journal of Geophysical Research: Earth Surface*, *116*(F2), doi:10.1029/2010JF001875.

Bates, P. D., M. S. Horritt, and T. J. Fewtrell (2010), A simple inertial formulation of the shallow water equations for efficient two-dimensional flood inundation modelling, *Journal of Hydrology*, *387*(1), doi:10.1016/j.jhydrol.2010.03.027.

Black, P. E. (1972), Hydrograph responses to geomorphic model watershed characteristics and precipitation variables, *Journal of Hydrology*, *17*(4), 309–329.

Costa, J. E., and J. E. O'Connor (1995), *Geomorphically Effective Floods*, pp. 45–56, American Geophysical Union, doi:10.1029/GM089p0045.

Culling, W. (1960), Analytical theory of erosion, *The Journal of Geology*, *68*(3), 336–344.

de Almeida, G. A. M., P. D. Bates, J. E. Freer, and M. Souvignet (2012), Improving the stability of a simple formulation of the shallow water equations for 2-d flood modeling, *Water Resources Research*, *48*(5), doi:10.1029/2011wr011570.

Deal, E., A.-C. Favre, and J. Braun (2017), Rainfall variability in the himalayan orogen and its relevance to erosion processes, *Water Resources Research*, doi:10.1002/2016WR020030.

Deal, E., G. Botter, and J. Braun (2018), Understanding the role of rainfall and hydrology in determining fluvial erosion efficiency, *Journal of Geophysical Research: Earth Surface*, *123*, doi:10.1002/2017JF004393.

DiBiase, R. A., and K. X. Whipple (2011), The influence of erosion thresholds and runoff variability on the relationships among topography, climate, and erosion rate, *Journal of Geophysical Research: Earth Surface*, *116*(F4), doi:10.1029/2011JF002095.

Eagleson, P. S. (1978), Climate, soil, and vegetation: 2. distribution of annual precipitation derived from observed storm sequences, *Water Resources Research*, *14*(5), 713–721, doi:10.1029/WR014i005p00713.

Grayman, W. M., and P. S. Eagleson (1969), Streamflow record length for modeling catchment dynamics, *Tech. rep.*, Hydrodynamics Laboratory, Department of Civil Engineering, Massachusetts Institute of Technology.

Guthrie, R. (2015), The catastrophic nature of humans, *Nature Geoscience*, *8*(6), 421–422, doi:10.1038/ngeo2455.

Hartshorn, K., N. Hovius, W. B. Dade, and R. L. Slingerland (2002), Climate-driven bedrock incision in an active mountain belt, *Science*, *297*(5589), 2036–2038, doi:10.1126/science.1075078.

Hawk, K. L. (1992), Climatology of station storm rainfall in the continental united states: Parameters of the bartlett-lewis and poisson rectangular pulses models, Master's thesis, Massachusetts Institute of Technology.

Hobley, D. E. J., J. M. Adams, S. S. Nudurupati, E. W. H. Hutton, N. M. Gasparini, E. Istanbulluoglu, and G. E. Tucker (2017), Creative computing with landlab: an open-source toolkit for building, coupling, and exploring two-dimensional numerical models of earth-surface dynamics, *Earth Surface Dynamics*, (5), 21–46, doi:10.5194/esurf-5-21-2017.

Hoober, D., T. Svoray, and S. Cohen (2017), Using a landform evolution model to study ephemeral gullying in agricultural fields: the effects of rainfall patterns on ephemeral gully dynamics, *Earth Surface Processes and Landforms*, *42*, 1213–1226, doi: 10.1002/esp.4090.

Howard, A. D. (1994), A detachment-limited model of drainage-basin evolution, *Water Resources Research*, *30*(7), 2261–2285, doi:10.1029/94wr00757.

Hunter, N. M., M. S. Horritt, P. D. Bates, M. D. Wilson, and M. G. F. Werner (2005), An adaptive time step solution for raster-based storage cell modelling of floodplain inundation, *Advances in Water Resources*, *28*(9), 975–991, doi:10.1016/j.advwatres.2005.03.007.

Istanbulluoglu, E., and R. L. Bras (2006), On the dynamics of soil moisture, vegetation, and erosion: Implications of climate variability and change, *Water Resources Research*, *42*(6), doi:10.1029/2005wr004113.

Ivanov, V. Y., R. L. Bras, and D. C. Curtis (2007), A weather generator for hydrological, ecological, and agricultural applications, *Water Resources Research*, *43*(10), doi: 10.1029/2006wr005364.

Jain, M. K., and V. P. Singh (2005), Dem-based modelling of surface runoff using diffusion wave equation, *Journal of Hydrology*, *302*(1-4), 107–126, doi: 10.1016/j.jhydrol.2004.06.042.

Jain, M. K., U. C. Kothyari, and K. G. R. Raju (2004), A gis based distributed rainfall-runoff model, *Journal of Hydrology*, *299*(1), 107–135, doi:10.1256/qj.02.97.

Julien, P. Y. (2010), *Erosion and sedimentation*, Cambridge University Press.

Lague, D. (2014), The stream power river incision model: evidence, theory and beyond, *Earth Surface Processes and Landforms*, *39*(1), 38–61, doi:10.1002/esp.3462.

Lague, D., N. Hovius, and P. Davy (2005), Discharge, discharge variability, and the bedrock channel profile, *Journal of Geophysical Research: Earth Surface*, *110*(F4), doi: 10.1029/2004jf000259.

Miller, A. J. (1990), Flood hydrology and geomorphic effectiveness in the central appalachians, *Earth Surface Processes and Landforms*, *15*(2), 119–134, doi: 10.1002/esp.3290150203.

Molnar, P. (2001), Climate change, flooding in arid environments, and erosion rates, *Geology*, *29*(12), 1071–1074, doi:10.1130/0091-7613(2001)029<1071:CCFIAE>2.0.CO;2.

Molnar, P., R. S. Anderson, G. Kier, and J. Rose (2006), Relationships among probability distributions of stream discharges in floods, climate, bed load transport, and river incision, *Journal of Geophysical Research: Earth Surface*, *111*(F2), doi:10.1029/2005jf000310.

Mügler, C., O. Planchon, J. Patin, S. Weill, N. Silvera, P. Richard, and E. Mouche (2011), Comparison of roughness models to simulate overland flow and tracer transport experiments under simulated rainfall at plot scale, *Journal of Hydrology*, *402*(1), 25–40, doi: 10.1016/j.jhydrol.2011.02.032.

Nearing, M. A., V. Jetten, C. Baffaut, O. Cerdan, A. Couturier, M. Hernandez, Y. Le Bissonnais, M. H. Nichols, J. P. Nunes, C. S. Renschler, V. Souchere, and K. van Oost (2005), Modeling response of soil erosion and runoff to changes in precipitation and cover, *Catena*, *61*(2), 131–154, doi:10.1016/j.catena.2005.03.007.

Ogden, F. L., and P. Y. Julien (1993), Runoff sensitivity to temporal and spatial rainfall variability at runoff place and small basin scales, *Water Resources Research*, *29*(8), 2589–2597, doi:10.1029/93WR00924.

Phillips, C. B., and D. J. Jerolmack (2016), Self-organization of river channels as a critical filter on climate signals, *Science*, *352*(6286), 694–697, doi:10.1126/science.aad3348.

Rengers, F. K., L. A. McGuire, J. W. Kean, D. M. Staley, and D. E. J. Hobley (2016), Model simulations of flood and debris flow timing in steep catchments after wildfire, *Water Resources Research*, doi:10.1002/2015WR018176.

Rossi, M. W., K. X. Whipple, and E. R. Vivoni (2016), Precipitation and evapotranspiration controls on daily runoff variability in the contiguous united states and puerto rico, *Journal of Geophysical Research: Earth Surface*, *121*, 128–145, doi:10.1002/2015JF003446.

Snyder, F. F. (1938), Synthetic unit-graphs, *Eos, Transactions American Geophysical Union*, *19*(1), 447–454.

Snyder, N. P., K. X. Whipple, G. E. Tucker, and D. J. Merritts (2003), Importance of a stochastic distribution of floods and erosion thresholds in the bedrock river incision problem, *Journal of Geophysical Research: Solid Earth*, *108*(B2), doi:10.1029/2001JB001655.

Sólyom, P. B., and G. E. Tucker (2004), Effect of limited storm duration on landscape evolution, drainage basin geometry, and hydrograph shapes, *Journal of Geophysical Research: Earth Surface*, *109*, doi:10.1029/2003jf000032.

Sorensen, C. S., and B. J. Yanites (2019), Latitudinal trends in modern fluvial erosional efficiency along the andes, *Geomorphology*, *329*, 170 – 183, doi: https://doi.org/10.1016/j.geomorph.2018.12.030.

Tucker, G. E. (2004), Drainage basin sensitivity to tectonic and climatic forcing: Implications of a stochastic model for the role of entrainment and erosion thresholds, *Earth Surface Processes and Landforms*, *29*(2), 185–205, doi:10.1002/esp.1020.

Tucker, G. E., and R. L. Bras (2000), A stochastic approach to modeling the role of rainfall variability in drainage basin evolution, *Water Resources Research*, *36*(7), 1953–1964, doi: 10.1029/2000WR900065.

Tucker, G. E., and G. R. Hancock (2010), Modelling landscape evolution, *Earth Surface Processes and Landforms*, *35*(1), 28–50, doi:10.1002/esp.1952.

Tucker, G. E., and R. L. Slingerland (1994), Erosional dynamics, flexural isostasy, and long-lived escarpments - a numerical modeling study, *Journal of Geophysical Research: Solid Earth*, *99*(B6), 12,229–12,243, doi:10.1029/94jb00320.

Turowski, J. M., N. Hovius, A. Wilson, and M. J. Horng (2008), Hydraulic geometry, river sediment and the definition of bedrock channels, *Geomorphology*, *99*(1), 26–38, doi: 10.1016/j.geomorph.2007.10.001.

Willgoose, G., R. L. Bras, and I. Rodriguez-Iturbe (1991), A coupled channel network growth and hillslope evolution model 1. theory, *Water Resources Research*, *27*(7), 1671–1684, doi:10.1029/91wr00935.

Wolman, M. G., and R. Gerson (1978), Relative scales of time and effectiveness of climate in watershed geomorphology, *Earth surface processes*, *3*(2), 189–208.

Wolman, M. G., and J. P. Miller (1960), Magnitude and frequency of forces in geomorphic processes, *The Journal of Geology*, *68*(1), 54–74.